

GaAs-Based Nanoneedle Light Emitting Diode and Avalanche Photodiode Monolithically Integrated on a Silicon Substrate

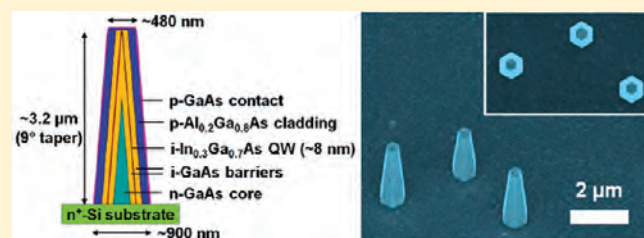
Linus C. Chuang,[†] Forrest G. Sedgwick,[†] Roger Chen, Wai Son Ko, Michael Moewe, Kar Wei Ng, Thai-Truong D. Tran, and Connie Chang-Hasnain*

Department of Electrical Engineering and Computer Sciences, University of California at Berkeley, Berkeley, California 94720, United States

S Supporting Information

ABSTRACT: Monolithic integration of III–V compound semiconductor devices with silicon CMOS integrated circuits has been hindered by large lattice mismatches and incompatible processing due to high III–V epitaxy temperatures. We report the first GaAs-based avalanche photodiodes (APDs) and light emitting diodes, directly grown on silicon at a very low, CMOS-compatible temperature and fabricated using conventional microfabrication techniques. The APDs exhibit an extraordinarily large multiplication factor at low voltage resulting from the unique needle shape and growth mode.

KEYWORDS: Nanoneedle, nanowire, III–V on Si, CMOS compatible, LED, APD



CMOS integrated circuits are based on silicon, while semiconductor lasers and a majority of optoelectronic devices use III–V compound semiconductors. Massively scalable integration of the two, which would simplify system designs and enable many applications, has proven difficult. Epitaxial growth of III–V materials on silicon substrates is the most direct and scalable route to integration. However, high-quality III–V materials typically require high synthesis temperatures which exceed the CMOS thermal budget of 400–450 °C. In addition, most III–V compound materials have significant mismatches of crystal lattice constants and thermal expansion coefficients with silicon, which result in defect-rich materials with major limitations on device performance, cost, and reliability.^{1–3} Techniques like wafer bonding have yielded high-quality III–V devices on silicon, including semiconductor lasers.^{4–7} However, there are significant challenges in applying this technique to finished CMOS wafers with diverse terrain and materials. The recent development of III–V nanowire growth on silicon is very promising to overcome the challenges of lattice mismatch and process incompatibility.^{8–12} Single crystalline InP and GaAs nanowires on silicon have been reported.^{8–10} III–V nanowire-based devices, on silicon or other substrates, have recently become a very active research field.^{13–17}

In this paper, we report room-temperature (RT) operation of GaAs core–shell nanoneedle avalanche photodiodes (APDs) and InGaAs/GaAs light emitting diodes (LEDs), all as-grown on silicon substrates and built using existing microfabrication techniques. The GaAs nanoneedles are grown on silicon using a new, catalyst-free growth mode at low (400 °C) growth temperature, facilitating CMOS compatibility.^{18,19} The nanoneedles

are very high quality single-crystalline III–V structures with sharp (2–5 nm) tips and robust submicrometer roots that make them suitable for top-down processing. Their size scales with growth time. The nanoneedle APD attains an extraordinarily high current gain of 263 with only 8 V bias. The gain has a reasonably linear dependence on voltage, making it less susceptible to breakdown damage. The nanoneedle LED exhibits a bright RT electroluminescence (EL) with a 64 nm line width (at 1128 nm) under a 3 μ A current injection. Both results are comparable to state-of-the-art discrete III–V planar devices.^{20–22} The nanoneedle APD has a substantially lower bias voltage than planar APDs, which typically have bias voltages greater than 20 V for a gain greater than 100.²¹ These preliminary achievements underscore the immense promise of nanoneedle-based optoelectronic devices.

The basic growth template of the devices in this paper is the GaAs nanoneedle, as shown by a scanning electron microscope (SEM) picture in Figure 1a. The nanoneedles are grown epitaxially on (111) Si by a metal–organic chemical vapor deposition (MOCVD) system used commercially for growing thin films. The growth temperature is 400 °C. The precursors are triethylgallium (TEGa) and *tert*-butylarsine (TBA). TEGa and TBA are chosen for their relatively low decomposition temperatures (300 and 380 °C, respectively),^{23,24} which facilitate the low-temperature GaAs nanoneedle growth. Typical TEGa and TBA mole fractions are 1.12×10^{-5} and 5.42×10^{-4} , respectively, in

Received: August 24, 2010

Revised: November 14, 2010

Published: December 21, 2010

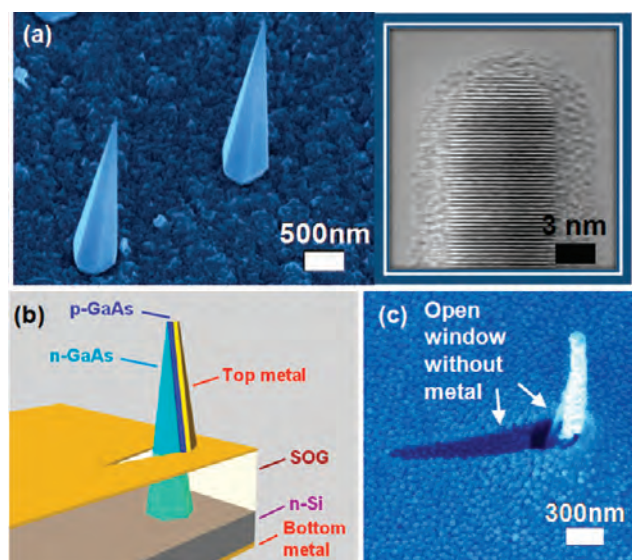


Figure 1. Nanoneedle photodiode materials and devices. (a) 30° tilt SEM image of as-grown nanoneedles. The nanoneedles are vertical to the substrate. Also shown is a TEM image of a nanoneedle tip showing radius of curvature smaller than 5 nm. The nanoneedle base is ~ 600 nm with a $\sim 7^\circ$ taper angle hence resulting in a needle-like high aspect ratio. (b) Nanoneedle photodiode device schematics. Each device is defined by a $200 \mu\text{m} \times 200 \mu\text{m}$ top p-metal contact and consists of 30–50 p–n GaAs nanoneedles on an n-type silicon substrate. One side of the nanoneedles is intentionally left uncoated with metal for optical coupling. (c) 30° tilt SEM image of a single nanoneedle in an as-fabricated photodiode device.

a 12 L/min hydrogen carrier gas flow. The reactor pressure is kept at 76 Torr. This growth condition results in GaAs nanoneedles with $\sim 4 \mu\text{m}$ in length for 1 h growth. Trimethylaluminum is added for AlGaAs growth. n-type and p-type doping are achieved by adding disilane and diethylzinc dopant sources, respectively.

Nanoneedle growth is initiated by spontaneous, catalyst-free clustering of hexagonal pyramid nanoneedle “seeds” on a roughened surface.^{18,19} Additional layers of material are subsequently deposited along the sides of the pyramids in a core–shell mode. The needles grow as wurtzite with the central axis along the [0001] crystal direction and normal to the (111) Si plane.^{18,19} The tip of the needle has a 2–5 nm radius of curvature (as seen in Figure 1a) and the body has a measured taper angle of 6–9°. A distinct feature of these novel structures is that this high aspect ratio is formed from the very beginning of nanoneedle growth (see Supporting Information). Furthermore, the length and base diameter scale proportionally with growth time. Hence the growth time may be extended to obtain larger nanoneedles with a sub-micrometer base, substantial enough for typical microfabrication processes like contact lithography.

The core–shell nanoneedle growth mode facilitates easy fabrication of p–n photodiodes, grown and fabricated into $200 \mu\text{m}$ square devices containing 30–50 nanoneedles each. The growth starts with an n-doped GaAs core (Si doped, $\sim 10^{17}/\text{cm}^3$), followed by a p-doped shell (Zn doped, $\sim 10^{18}/\text{cm}^3$) on an n-type (111) silicon substrate ($\sim 10^{15}/\text{cm}^3$). The nominal nanoneedle core radius, shell thickness, and height are 250 nm, 50 nm, and $4 \mu\text{m}$, respectively. The p-GaAs doping concentration is estimated by growing p-GaAs nanoneedles on p-type silicon, measuring the nanoneedle resistance, and calculating the

hole concentration using the bulk material hole mobility. The Zn doping concentration is nearly the same as the hole concentration since Zn is a shallow p-type dopant for GaAs.²⁵ n-type doping concentrations higher than $\sim 10^{18}/\text{cm}^3$ can be estimated the same way. However, making a good Ohmic contact is more difficult at lower concentrations. Therefore, the $\sim 10^{17}/\text{cm}^3$ n-type doping concentration is estimated optically by comparing the 4 K photoluminescence (PL) peak wavelength to that of an undoped nanoneedle. PL peak wavelength red shifts as the doping concentration increases due to band gap narrowing.²⁶ Figure 1b shows a schematic diagram of the nanoneedle photodiode, fabricated using standard photolithography and metallization processes. As-grown needles have a p-layer coated all around the n-doped core (see Figure S.1a in the Supporting Information). To make a diode without current leakage, it is important to remove the connecting path between the p-layer on the needle and the substrate. In addition, it is important to leave part of the needle uncovered by metal to facilitate light collection. The resulting structure has the top p-contact cover only one side of the p-layer, leaving the other side of the needle open for light collection as shown in Figure 1b. The fabrication steps start with a photoresist coating ($\sim 1.1 \mu\text{m}$) onto an as-grown p–n nanoneedle wafer, followed by a soft bake. The photoresist coverage of the upper part of the nanoneedles is very minimum due to the low photoresist viscosity and the high nanoneedle aspect ratio. This minimum photoresist residue on the protruding part of the nanoneedles is easily removed by an unmasked O_2 -plasma ash. A thin Ti/Au film ($\sim 5/15$ nm) is then deposited onto only one side of the nanoneedles by a 30° angled deposition. The photoresist is stripped, leaving the metal film only on the upper portion of the nanoneedles. This Ti/Au film is then used as an etching mask for timed wet etching the connection between the p-type nanoneedle shell and the n-type silicon substrate, which is a current leakage path. Next, spin-on-glass (SOG) ($\sim 1.3 \mu\text{m}$ thick) is applied to surround the nanoneedles to provide a platform for the top metal contact. The SOG is cured at 300 °C for 2 h. An unmasked CF_4/O_2 plasma etch is performed to remove the SOG residue on the protruding part of the nanoneedles. A standard, contact-photolithography step is then carried out to define the top p-metal into $200 \mu\text{m} \times 200 \mu\text{m}$ square regions. A thicker Ti/Au film ($\sim 10/120$ nm) is then deposited (also with a 30° tilt), onto the previous thin metal on nanoneedles and onto the SOG surface, as the top p-metal contact. A photoresist lift-off process is done to complete the p-metal contact definition. Finally, n-metal contact is layered onto the entire backside of the n-silicon substrate. The 30° angled top p-metal deposition process leaves shadows without any metal next to each nanoneedle, as clearly seen in the SEM image in Figure 1c. A most interesting observation is that light shone on this triangular shadow area is also collected by the nanoneedle detector, as discussed in the following section

As a control experiment to illustrate doping incorporation and Ohmic semiconductor/metal contact, p-nanoneedles on p-silicon and n-nanoneedles on n-silicon were first fabricated, respectively. Their linear I – V characteristics at RT were observed (see Supporting Information).

An excellent and nearly ideal current–voltage diode characteristic is achieved with the nanoneedle diode without illumination (dark) as illustrated by Figure 2a. A sharp turn-on voltage of ~ 1.4 V is obtained. A reasonably small reverse-bias dark current (< 100 nA) is seen up to -5 V, followed by a breakdown at -11 V. This ideal diode characteristic of GaAs on silicon is comparable

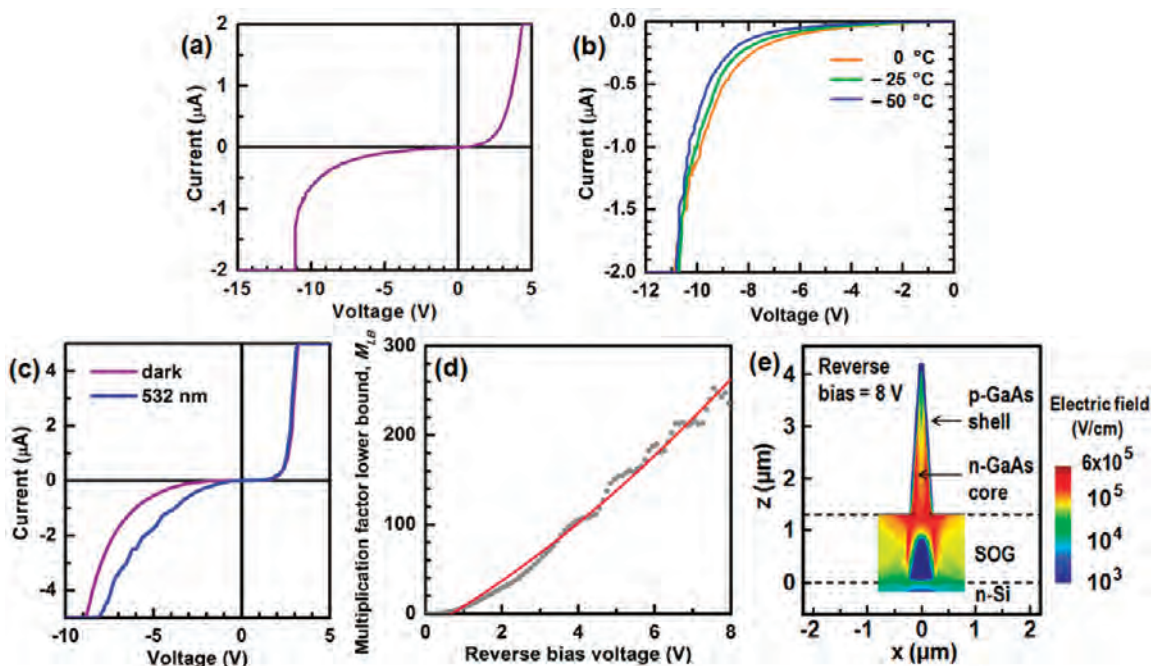


Figure 2. Nanoneedle photodiode device characterization. (a) Dark current of a nanoneedle photodiode. The device shows sharp turn on at ~ 1.4 V and a breakdown at -11 V. (b) Temperature-dependent dark I - V at the reversion bias region. The dark I - V for 0 , -25 , and -50 $^{\circ}\text{C}$ intersect each other at the breakdown voltage indicating the avalanche breakdown mechanism. (c) Measured dark and light I - V curves of a device under a 532 nm laser illumination with 0.26 W/cm^2 irradiance. (d) Current multiplication factor lower bound, M_{LB} (see text for definition), of a device. The M_{LB} at -8 V is as high as 263 , indicating a strong current multiplication behavior. (e) Electric field distribution inside a nanoneedle photodiode device at -8 V bias. Regions with electric field greater the breakdown field (4.5×10^5 V/cm) are seen, which contribute to the impact ionization and hence the avalanche multiplication.

to other high-quality III-V-on-silicon diodes fabricated by wafer-bonding techniques.^{27,28}

To investigate the device breakdown mechanism, temperature-dependent dark current characterizations were conducted as shown in Figure 2b. The dark I - V curves for different temperatures intersect at -11 V. Since reverse bias current below breakdown increases with temperature,²⁹ the intersection of the I - V curves indicates that the breakdown voltage must also increase with temperature. This is a clear signature of the avalanche as opposed to tunneling effect for the breakdown mechanism.³⁰

The APD's optical response is first characterized with a 532 nm laser. The illumination spot size is focused down to ~ 200 μm in diameter and is carefully adjusted to be totally confined within the 200 $\mu\text{m} \times 200$ μm top p-metal pad area. As a consequence, light can only be coupled into the device through the uncoated side of the nanoneedles and the triangular metal-free region next to the nanoneedles (see Figure 1b). Only these areas account for the incident photon flux since the thick Ti/Au metal blocks the light for all the other areas. The measured dark and light I - V curves are shown in Figure 2c. The photocurrent is obtained by subtracting the dark I - V curve from all I - V data taken under illumination. The current multiplication factor M is calculated based on the following equation.³¹

$$M = \frac{(I_p/q)}{\eta_i[\Phi_p A(1-R)]} \quad (1)$$

where I_p , q , η_i , Φ_p , A , and R are the photocurrent, electron charge, internal quantum efficiency, incident photon flux estimated from the exposed (metal-free) area, and the device reflectivity, respectively. Here, the numerator I_p/q is simply the

number of electrons measured by the APD per unit time. The denominator is multiplication of internal quantum efficiency and the photons collected by the device per unit time $\Phi_p A(1-R)$. An estimate of R is obtained by calculating the reflectivity of the spin-on-glass/Si layer (see Supporting Information). A conservative estimate of the current gain, noted as the lower bound of M , M_{LB} , is reached by setting η_i to a maximum value of 100%.

The experimental lower-bound of current gain M_{LB} is plotted as a function of bias voltage in Figure 2d, along with a second-order polynomial fit shown in red. It is noted that the gain is quite substantial at very low voltages, reaching 29 at -2 V. At -8 V bias, the gain is as high as ~ 263 . This is very large comparing to a state-of-the-art planar Ge/Si APD which has a gain of ~ 14 at -24 V,²⁰ and a planar InGaAs/Si APD which has a gain of 100 at -24 V.²¹ Because power dissipation is the product of photocurrent and bias voltage, this reduction of voltage for the same gain is vital for densely integrated devices where power and thermal budget are at a premium. In addition, the M_{LB} -voltage dependence is nearly linear, in sharp contrast to the exponential dependence of conventional APDs.³¹ This is highly advantageous to avoid device burn-out. These data suggest that nanoneedles may enable APD devices that pack more densely and demand smaller operating voltage than existing designs.

To investigate the origin of the uniquely low bias voltage, we performed three-dimensional simulation using a commercial multiphysics device simulator (Sentaurus Device). Figure 2e shows the electric field distribution inside a nanoneedle photodiode at -8 V bias. Regions with electric field greater than the breakdown field (4.5×10^5 V/cm) are clearly seen in red, supporting avalanche multiplication via impact ionization as the current gain mechanism. The curved, cylinder-like p-n junction

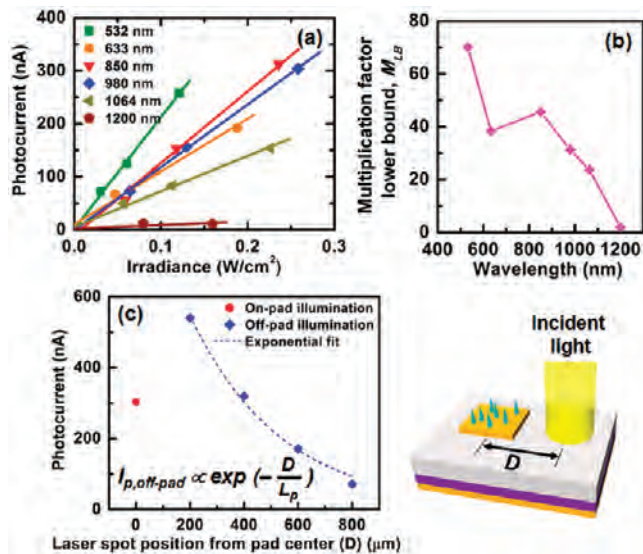


Figure 3. Illumination wavelength dependence of photoresponse of a nanoneedle photodiode. (a) Photocurrent as a function of irradiance for various wavelengths. The below GaAs band gap absorption (>870 nm) and nearly zero 1200 nm response imply that, in addition to the GaAs nanoneedles, the silicon substrate also participates in the light absorption. (b) Current multiplication factor lower bound (M_{LB}) as a function of wavelength. The device was biased at -10 V. (c) Photocurrent as a function of laser spot position. The illumination is a 980 nm, 0.26 W/cm^2 laser. This wavelength allows the investigation of the silicon-substrate-related absorption. The laser spot position (D) is measured from the center of the pad (see schematic). The off-pad photocurrent shows exponential decay (fitting equation shown on figure, see text for details) suggesting that the photocurrent is limited by the hole diffusion length in the n-type silicon substrate. The off-pad photocurrents ($I_{p,off-pad}$) are fitted with a hole diffusion length (L_p) of ~ 340 μm , which is in good agreement to the literature.

in a nanoneedle is thought to enhance the electric field and hence reduce the breakdown voltage via the lighting rod effect.³² Since the radius of curvature of a nanoneedle is 3–300 nm from top to base, and the depletion junction width is calculated as ~ 1 μm , the radius to depletion width ratio ranges from 0.003 to 0.3. On the basis of this ratio, the breakdown voltage would be ranging approximately from 5% to 50% of that of a planar structure using the formula established by Baliga and Gandhi for cylindrically curved junctions.³²

Finally, both the irradiance and wavelength dependence of the responsivity are characterized for an APD biased at -10 V. Figure 3a shows the photocurrent versus irradiance for various wavelengths. A linear dependence is observed at all wavelengths over the irradiance range tested here, indicating device operation in the linear regime. The current multiplication factor lower bound, M_{LB} , as a function of illumination wavelength is calculated and plotted in Figure 3b. The responsivity is significant for photon energy below the GaAs band gap (>870 nm) and does not fall to zero until 1200 nm, which is below the band gap for silicon. This intriguing result indicates that photocarriers are generated not only in GaAs nanoneedles but also silicon substrate and subsequently collected and multiplied by the nanoneedles. The assertion is further verified by using an illumination wavelength (980 nm) below the GaAs band gap and moving the laser spot off the device, where there is no nanoneedle. Figure 3c plots the photocurrent as a function of distance of the laser spot from the center of the p-contact pad.

For distances greater than 200 μm , the laser spot is completely off the pad and carriers must diffuse from the laser spot to the reverse-biased nanoneedle junctions. This diffusion-limited off-pad photocurrent, $I_{p,off-pad}$ is fitted with the following exponential form

$$I_{p,off-pad} \propto \exp\left(-\frac{D}{L_p}\right) \quad (2)$$

where D is the laser spot position and L_p is the hole diffusion length in n-type silicon. By fitting the off-pad data points in Figure 3c, the diffusion length L_p is estimated as ~ 340 μm , which is in good agreement to the hole diffusion length for $\sim 10^{15}/cm^3$ n-type silicon.^{33–35} This verifies the role of the silicon substrate in the photoresponse. It is also noted that the 200 μm off-pad photocurrent is only ~ 1.8 times larger than the on-pad photocurrent while the photon flux is ~ 3300 times larger (no metal blocking the light coupling). In this case, the off-pad illumination and detection scheme is inefficient due to the very long distance for the carriers to diffuse from the illuminated silicon region to the needles. Nevertheless, with off-pad illumination, our device acts like a separate absorption and multiplication APD,³⁶ with holes being generated in the silicon substrate region and then transported and amplified in the GaAs nanoneedle region. It is the needle-shaped p–n junction and resulting base-to-tip electric field which allow this new carrier collection mechanism.

In addition to detection, nanoneedles also enable functionalities based on optical emission. As efficient light emission requires a heterostructure, we use a nanoneedle structure with an InGaAs quantum well (QW) active region sandwiched by GaAs barriers and an AlGaAs cladding layer. The growth starts with an n-type GaAs nanoneedle core (radius ~ 130 nm), followed by an ~ 85 nm i-GaAs inner barrier, an 8 nm $In_{0.3}Ga_{0.7}As$ QW, an outer ~ 85 nm i-GaAs barrier, a ~ 125 nm p- $Al_{0.2}Ga_{0.8}As$ cladding, and a ~ 20 nm p-GaAs contact layer to complete the growth (see Figure 4a). Te and Zn are the n- and p-type dopants, respectively, and both are in the $\sim 10^{18}/cm^3$ range. The incorporation of 30% indium in InGaAs layer (the QW layer) stops the vertical growth due to the high indium composition, which thus transforms the sharp nanoneedle to a flat-topped pillar (herein referred to as a nanopillar). The pillar structure is of great advantage for light emitting devices, facilitating better light collection and potential optical feedback for future demonstration of lasers. The as-grown nanopillar structures are shown in Figure 4b at both a 30° -tilt view and a top-down view. The nanopillars were fabricated into LED devices using the same processes as the nanoneedle photodiodes.

The RT current–voltage characteristics of a nanopillar LED are shown in Figure 4c. The device contacts ~ 15 nanopillars (estimated with optical microscopy). The I – V exhibits typical behavior of a p–n rectifying junction with a turn-on voltage at ~ 0.9 V. The reverse breakdown is between -4 and -5 V due to the very thin undoped layers. The light output power–current (L – I) curve has a linear behavior, shown in the inset, which is typical for a high-quality LED with no nonradiative defect states to be filled up.

Single-pillar EL is characterized at RT by a 750 mm imaging spectrometer coupled to an InGaAs CCD and shown in Figure 4d. The spectrum peaks at 1128 nm and has a full width at half-maximum (fwhm) of 64 nm at 3 μA current injection. This fwhm is quite narrow²² considering the line width broadening due to phonon scattering at RT.³⁷ The narrow fwhm testifies to the high material quality of the QW nanopillar structure.

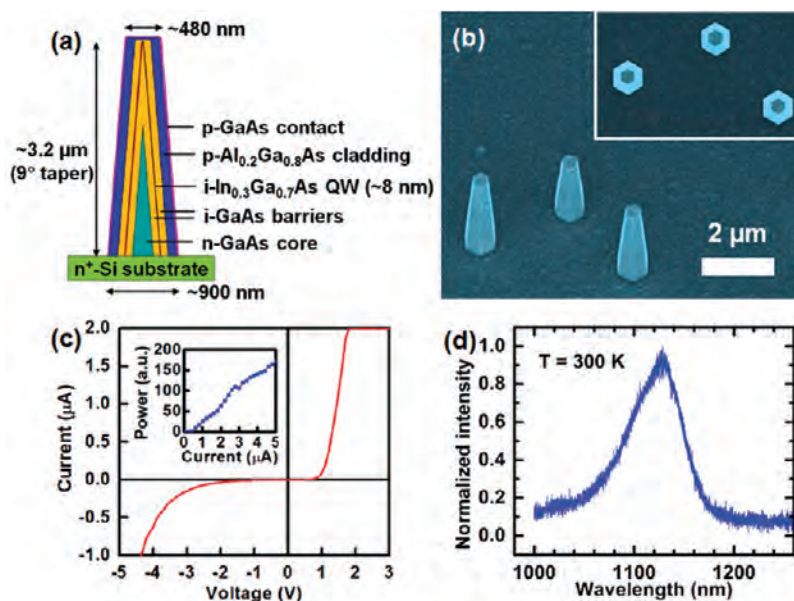


Figure 4. Nanopillar LED structure and optical properties. (a) Nanopillar LED structure design. The structure consists of a sharp n-GaAs nanoneedle core and a sharp i-GaAs inner nanoneedle barrier. The i- $\text{In}_{0.3}\text{Ga}_{0.7}\text{As}$ QW then stops the nanoneedle vertical growth, allowing further growth only in the lateral direction. This results in a flat-top nanopillar structure. The outer i-GaAs barrier, a p- $\text{Al}_{0.2}\text{Ga}_{0.8}\text{As}$ cladding and a final p-GaAs contact were all grown primarily in the lateral direction with very minimal top c -plane deposition. (b) 30° -tilt SEM image of as-grown nanopillar LED structures. Inset is the top-down view. Hexagonal nanopillar cross sections are clearly seen. (c) I - V characteristics of a nanopillar LED device contacting ~ 15 nanopillars. Inset is the L - I curve. The L - I dependence is linear. (d) RT EL spectrum of a nanopillar LED (peaked at 1128 nm). The EL was measured under a $3 \mu\text{A}$ current injection. The narrow fwhm of 64 nm testifies to the high material quality of the QW nanopillar structure.

In conclusion, we present high-quality APD and LED devices using a novel core-shell GaAs nanoneedle structure directly grown on (111) Si substrates. The growth was done at a CMOS-compatible growth temperature of 400°C . These nanostructure-based APD and LED are fabricated using standard microfabrication processes including contact lithography, representing a major advance toward massive integration. The nanoneedle photodiode shows a very high and nearly linear current gain as a function of voltage, making the device very robust when integrated with circuits (easy to avoid run-away burn-out). We report a high current gain of 29 at -2 V and 263 at -8 V . The avalanche multiplication is likely due to the high electric field inside the tapered nanoneedle. The core-shell $\text{In}_{0.3}\text{Ga}_{0.7}\text{As}/\text{GaAs}$ QW nanopillar LED devices show a RT I - V curve with $\sim 0.9\text{ V}$ turn-on voltage and bright RT EL emission. Our results demonstrate for the first time the viability of a revolutionary new class of optoelectronic devices based on direct-band-gap III-V materials epitaxially grown on silicon in a CMOS compatible fashion and processed with standard top-down lithographic techniques.

ASSOCIATED CONTENT

Supporting Information. Further details on the time evolution of nanoneedle growth, the p-nanoneedles on p-Si and n-nanoneedles on n-Si substrates control experiments, and the SOG/Si multiplayer reflectivity. This material is available free of charge via the Internet at <http://pubs.acs.org>.

AUTHOR INFORMATION

Corresponding Author

*E-mail (C.C.-H.): cch@berkeley.edu.

Author Contributions

[†]These authors contributed equally to this work.

ACKNOWLEDGMENT

This work was supported by DARPA UPR Award HR0011-04-1-0040 and a DoD National Security Science and Engineering Faculty Fellowship via Naval Post Graduate School N00244-09-1-0013. The authors acknowledge the fellowship support from the UC Berkeley EECS Fellowship Program, NSF-IGERT Program, NDSEG Fellowship Program, and NSF Graduate Research Fellowship Program.

REFERENCES

- (1) Fang, S. F.; Adomi, K.; Iyer, S.; Morkoc, H.; Zabel, H.; Choi, C.; Otsuka, N. *J. Appl. Phys.* **1990**, *68*, R31.
- (2) Lum, R. M.; Klingert, J. K.; Bylisma, R. B.; Glass, A. M.; Macrander, A. T.; Harris, T. D.; Lamont, M. G. *J. Appl. Phys.* **1988**, *64*, 6727.
- (3) Matthews, J. W.; Blakeslee, A. E. *J. Cryst. Growth* **1974**, *27*, 118.
- (4) Lo, Y. H.; Bhat, R.; Hwang, D. M.; Chua, C.; Lin, C. H. *Appl. Phys. Lett.* **1993**, *62*, 1038.
- (5) Park, H.; Fang, A. W.; Kodama, S.; Bowers, J. E. *Opt. Express* **2005**, *13*, 9460.
- (6) Fang, A. W.; Park, H.; Cohen, O.; Jones, R.; Paniccia, M. J.; Bowers, J. E. *Opt. Express* **2006**, *14*, 9203.
- (7) Campenhout, J. V.; Rojo-Romeo, P.; Regreny, P.; Seassal, C.; Thourhout, D. V.; Verstuyft, S.; Ciocco, L. D.; Fedeli, J.-M.; Lagahe, C.; Baets, R. *Opt. Express* **2007**, *15*, 6744.
- (8) Martensson, T.; Svensson, C. P. T.; Wacaser, B. A.; Larsson, M. W.; Seifert, W.; Deppert, K.; Gustafsson, A.; Wallenberg, L. R.; Samuelson, L. *Nano Lett.* **2004**, *4*, 1987.
- (9) Chuang, L. C.; Moewe, M.; Chase, C.; Kobayashi, N. P.; Chang-Hasnain, C.; Crankshaw, S. *Appl. Phys. Lett.* **2007**, *90*, No. 043115.

- (10) Chuang, L. C.; Moewe, M.; Crankshaw, S.; Chang-Hasnain, C. *Appl. Phys. Lett.* **2008**, *92*, No. 013121.
- (11) Ertekin, E.; Greaney, P. A.; Chrzan, D. C.; Sands, T. D. *J. Appl. Phys.* **2005**, *97*, No. 114325.
- (12) Glas, F. *Phys. Rev. B* **2006**, *74*, No. 121302.
- (13) Tomioka, K.; Motohisa, J.; Hara, S.; Hiruma, K.; Fukui, T. *Nano Lett.* **2010**, *10*, 1639.
- (14) Svensson, C. P. T.; Martensson, T.; Tragardh, J.; Larsson, C.; Rask, M.; Hessman, D.; Samuelson, L.; Ohlsson, J. *Nanotechnology* **2008**, *19*, 305201.
- (15) Wei, W.; Bao, X.-Y.; Soci, C.; Ding, Y.; Wang, Z.-L.; Wang, D. *Nano Lett.* **2009**, *9*, 2926.
- (16) Yang, C.; Barrelet, C. J.; Capasso, F.; Lieber, C. M. *Nano Lett.* **2006**, *6*, 2929.
- (17) Hayden, O.; Agarwal, R.; Lieber, C. M. *Nat. Mater.* **2006**, *5*, 352.
- (18) Moewe, M.; Chuang, L. C.; Crankshaw, S.; Chase, C.; Chang-Hasnain, C. *Appl. Phys. Lett.* **2008**, *93*, No. 023116.
- (19) Moewe, M.; Chuang, L. C.; Crankshaw, S.; Ng, K. W.; Chang-Hasnain, C. *Opt. Express* **2009**, *17*, 7831.
- (20) Kang, Y.; Liu, H.-D.; Morse, M.; Paniccia, M. J.; Zadka, M.; Litski, S.; Sarid, G.; Pauchard, A.; Kuo, Y.-H.; Chen, H.-W.; Zaoui, W. S.; Bowers, J. E.; Beling, A.; McIntosh, D. C.; Zheng, X.; Campbell, J. C. *Nat. Photonics* **2008**, *3*, 59.
- (21) Hawkins, A. R.; Wu, W.; Abraham, P.; Streubel, K.; Bowers, J. E. *Appl. Phys. Lett.* **1997**, *70*, 303.
- (22) Blondelle, J.; Neve, H. D.; Demeester, P.; Daele, P. V.; Borghs, G.; Baets, R. *Electron. Lett.* **1994**, *30*, 1787.
- (23) Lee, P. W.; Omstead, T. R.; McKenna, D. R.; Jensen, K. F. *J. Cryst. Growth* **1987**, *85*, 165.
- (24) Larsen, C. A.; Buchan, N. I.; Li, S. H.; Stringfellow, G. B. *J. Cryst. Growth* **1989**, *94*, 663.
- (25) Sze, S. M.; Irvin, J. C. *Solid-State Electron.* **1968**, *11*, 599.
- (26) Jain, S. C.; Roulston, D. J. *Solid-State Electron.* **1991**, *34*, 453.
- (27) Ejeckam, F. E.; Chua, C. L.; Zhu, Z. H.; Lo, Y. H.; Hong, M.; Bhar, R. *Appl. Phys. Lett.* **1995**, *67*, 3936.
- (28) Ohira, K.; Kobayashi, K.; Iizuka, N.; Yoshida, H.; Ezaki, M.; Uemura, H.; Kojima, A.; Nakamura, K.; Furuyama, H.; Shibata, H. *Opt. Express* **2010**, *18*, 15440.
- (29) Blanks, D. K.; Beck, J. D.; Kinch, M. A.; Colombo, L. *J. Vac. Sci. Technol., A* **1988**, *6*, 2790.
- (30) Sze, S. M. *Physics of Semiconductor Devices*; John Wiley & Sons: New York, 1981.
- (31) Chuang, S. L. *Physics of Optoelectronic Devices*; John Wiley & Sons: New York, 1995.
- (32) Baliga, B. J.; Ghandhi, S. K. *Solid-State Electron.* **1976**, *19*, 739.
- (33) Passari, L.; Susi, E. *J. Appl. Phys.* **1983**, *54*, 3935.
- (34) Burk, D. E.; De La Torre, V. *IEEE Electron Device Lett.* **1984**, *EDL-5*, 231.
- (35) Pierret, R. F. *Semiconductor Device Fundamentals*; Addison Wesley: Reading, MA, 1996.
- (36) Nishida, K.; Taguchi, K.; Matsumoto, Y. *Appl. Phys. Lett.* **1979**, *35*, 251.
- (37) Lee, J.; Koteles, E. S.; Vassell, M. O. *Phys. Rev. B* **1986**, *33*, 5512.